



Universitat
de les Illes Balears

MASTER'S THESIS

Perturbations propagation in self-organized patterns

David Abella Bujalance

Master's Degree in Physics of Complex Systems

(Specialization/Pathway in Complex Systems)

Centre for Postgraduate Studies

Academic Year 2019/2020

Perturbations propagation in self-organized patterns

David Abella Bujalance

Master's Thesis

Centre for Postgraduate Studies

University of the Balearic Islands

Academic Year 2019/2020

Keywords:

Self-organization, patterns, spatiotemporal dynamics, perturbation.

Thesis Supervisor's Name: Dr. Damià Gomila Villalonga

To my family and friends, for all their support in my formative years.

Acknowledgments

Without the supervision and constant help from my supervisor Dr. Damià Gomila, this work would not have been possible. Therefore, I would like to sincerely acknowledge him for all the hours expended and all the guidance and advisement. Also, a special thank Prof. Thorsten Ackemann for the shared information about the state of the art of experimental studies related this same phenomena.

I want to thank this thesis to my school friends: Alberto, Marcel, Jaume S. and Jaume V. for all cheering and support during this last months, getting me distracted but also cheering me up to do a great job. Also, a very special thank to Rosa and Pau for being patient with my frustrations along the way and always bring a smile to my face. Moreover, I am grateful for my friends during this master in Physics of Complex Systems for the great moments shared along the year.

Finally, I want to acknowledge my family for all support and love they have always given to me.

David Abella Bujalance

Abstract

In optical cavities, self-organized patterns can emerge because of diffraction and optical nonlinearities. This phenomena can be used to induce self-organization of an atomic cloud. Thus, this pattern can be understood as a lattice of cold atomic groups coupled by diffraction. From this point of view, there is an analogy between this system and a lattice of atoms in a solid. From solid-state theory, a perturbation of the position of an atom in the lattice leads to a sound wave that propagates along the solid.

Following this idea, our aim in this work is to study the response of a self-organized pattern to a localized perturbation at one of the pattern peaks. Since the system is highly dissipative, we first study the dynamics of this system in order to choose a set of parameters close to a critical point in such a way that gain can counterbalance dissipation allowing the perturbations to propagate longer. Next, we run numerical simulations of our differential equation, taking as an initial condition the perturbed pattern. From the numerical results we extract propagation features such as the velocity, period, symmetry, etc.

Finally, we characterize the perturbation propagation theoretically, and compare the analytical results with the numerical integration.

Resum

En cavitats òptiques, s'ha vist que poden emergir patrons autoorganitzats gràcies al fenomen de difracció i als efectes òptics no lineals. Aquest fenomen es pot utilitzar per induir autoorganització en un núvol d'àtoms freds. Aquests patrons es poden entendre com una xarxa de grups d'àtoms freds acoblats per la difracció. Des d'aquest punt de vista, podem fer una analogia d'aquest sistema amb el d'una xarxa d'àtoms en un sòlid. Com ens diu la teoria d'estat sòlid, una pertorbació de la posició d'un àtom a la xarxa provoca una ona de so que es propaga al llarg del sòlid.

Seguint amb aquesta idea, el nostre propòsit en aquest treball és estudiar la resposta d'un patró hexagonal autoorganitzat a una pertorbació localitzada a un dels pics del patró. Com el sistema és altament dissipatiu, primer estudiem la dinàmica del sistema per escollir una combinació de paràmetres a prop del punt crític de forma que el guany pugui contrarestar la dissipació per tal que la pertorbació es propagui més lluny. A continuació, correm una simulació numèrica de la nostra equació, agafant com a condició inicial el patró ja pertorbat. D'aquests resultats numèric en podrem extreure característiques de la propagació com la velocitat, el període, la simetria, etc.

Finalment, caracteritzem la pertorbació teòricament i comparem els resultats analítics amb la integració numèrica.

Contents

Acknowledgments	iii
Abstract	v
1 Introduction	1
2 Model: the Lugiato-Lefever equation	5
2.1 Linear stability analysis	6
2.2 Hexagonal patterns	7
2.3 Secondary bifurcations of stationary hexagonal patterns	9
3 Perturbation propagation	17
3.1 Characterization of the perturbation	17
3.2 Numerical results	17
3.3 Theoretical analysis	24
Discussion and concluding remarks	29
Appendix	31
Bibliography	37

Chapter 1

Introduction

We define pattern formation as the spontaneous emergence of spatiotemporal structures in nonlinear systems driven far from equilibrium [1]. The spatial structuring is consequence of an interplay between nonlinearities and spatial coupling mechanisms as diffusion. An interesting example are optical systems, where it is well known that optical nonlinearities and diffraction can induce a full range of different patterns. This emergence takes place inside the medium through light intensity modulations.

This phenomena can be used to induce spontaneous self-organization in atomic media cold enough for optical intensities to overcome thermal effects. The crucial new ingredient in cold atoms is the existence of macroscopic matter transport processes due to dipole forces, leading to a density organization without the need for an intrinsic optical nonlinearity [2]. When dynamics of light are coupled with center-of-mass degrees of freedom of atoms, the dynamics become nonlinear and, above a certain value of the intensity injected, a transition is observed from a spatially homogeneous state to a long-range ordered state. This phenomena of optomechanical self-structuring has been reported for many different situations: recoil-induced resonances [3], superradiant Rayleigh scattering [4], collective atomic recoil lasing (CARL) [5] and in transversally pumped cavities [2]. An example of this last one is shown in Fig. 1.1, where the emergence of a pattern in the pump beam is accompanied by the self structuring of the atomic cloud, measured by the probe beam (see experimental set-up Fig.1.1b).

In order to describe the possible solutions in a theoretical way, we use the dynamical systems theory including methods of nonlinear dynamics and bifurcation theory such as amplitude equations, that describe the dynamics close to the critical points. However, these analytical tools are limited. For our case, if the pattern solution undergoes secondary bifurcations far from the pattern formation instability, dynamics will not be reproduced by amplitude equations. Nevertheless, other models are reported in literature to model this same problem. In Ref. [6], the self-organization is understood as a synchronization transition in a fully connected network of fictitious oscillators described by the Kuramoto model [7].

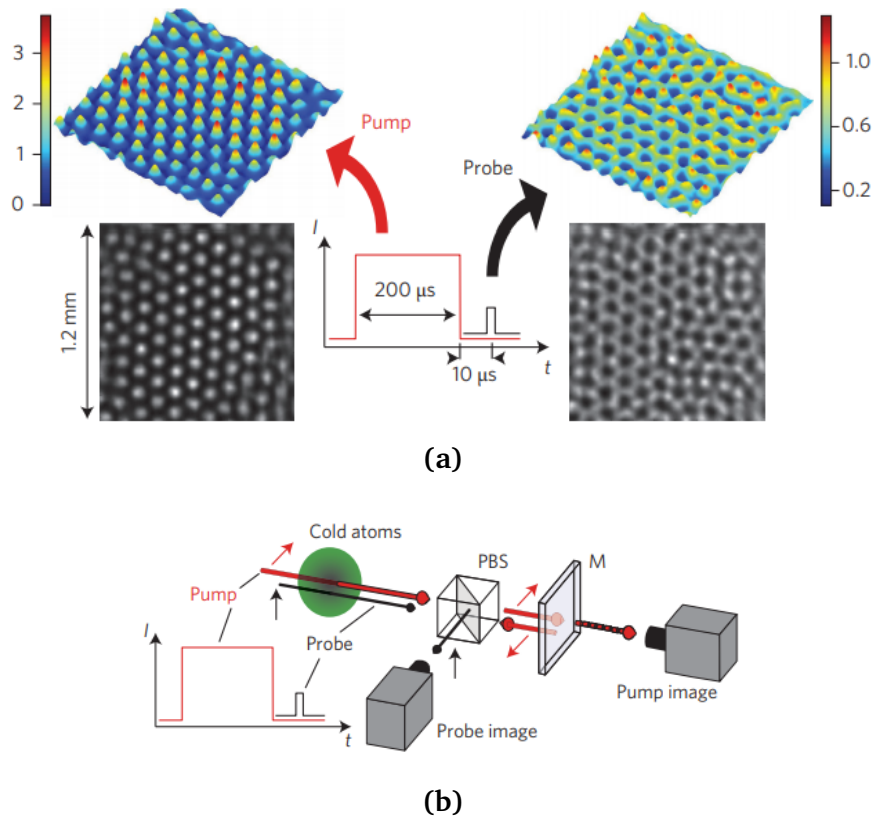


Figure 1.1: Self-organization observation and set-up: (a) Transmission images (normalized to intensities transmitted in the absence of atomic cloud) recorded with pump and probe. (b) Experimental set-up and timing diagram for pump and probe pulses. M , mirror; PBS , polarizing beam-splitter. From Ref. [2].

One of the most simple systems to display pattern formation is a ring cavity filled with a nonlinear Kerr medium¹. As explained in Chapter 2, a nonlinear analysis of this model predicts the formation of hexagonal patterns for a particular set of parameters. A linear stability analysis of this pattern solution shows the different instabilities of this solution against periodic perturbations.

With a further analysis one can show this system can also support localized structures (Kerr Cavity Solitons) [9], which can be basically considered as isolated peaks of the hexagonal pattern. Therefore, for certain parameter values the pattern can be understood as an hexagonal lattice of coupled solitons. This coupling between neighbours peaks comes from diffraction.

¹Medium which optical response is described by a Kerr nonlinearity. This is reflected with a polarization term $P = \chi^{(3)}EEE$. [8]

From this last idea comes the motivation of this work, because our self-organized pattern of a cold atomic gas, consequence of an optomechanical process, can be interpreted as a lattice of cold atomic groups, which are coupled and undergo similar instabilities for a given value of the intensity injected. Therefore, we can make an analogy with a two-dimensional lattice of atoms or molecules in a solid which can be studied in terms of condensed matter physics.

It is known that a perturbation of one atom in the lattice, due to the periodicity of Bloch functions, creates a sound wave that propagates along the solid. Our aim in this work is to reproduce a similar phenomena in self-organized patterns and give a description of the perturbation propagation behaviour in a theoretical way.

Chapter 2

Model: the Lugiato-Lefever equation

The mean field equation describing a Kerr medium in a cavity with flat mirrors and driven by a coherent plane wave is one of the models to describe spatial structures in nonlinear optics. The differential equation that governs this dynamics is the, so called, Lugiato-Lefever equation (2.1) [10]. We chose this model for our analysis because it has very rich dynamics and exhibits several interesting bifurcations.

In the mean field limit, the dynamics of the scaled slowly varying amplitude of the electric field $E(\vec{x}, t)$ follow the equation:

$$\partial_t E = -(1 + i\eta\theta)E + i\nabla^2 E + E_0 + i\eta|E|^2 E \quad (2.1)$$

where E_0 is the input field, θ is the cavity detuning, $\eta = \pm 1$ determines if the non-linearity type is focusing (+) or defocusing (-), and ∇^2 is the transverse Laplacian. This equation has been normalized by the cavity decay rate. This model is appropriate for cavities where we can assume that only one longitudinal mode is excited.

This model, besides the hexagonal pattern formation, exhibits a set of possible solutions depending on parameters η and θ . In the self-focusing case, for pump intensities above a certain value, hexagonal patterns emerge while stripe patterns are unstable. However, in the self-defocusing case, patterns are not formed. Extensions of this model can also lead to stripe patterns in this self-defocusing case or even localized structures.

The homogeneous stationary solution E_s of equation Eq. (2.1) is given by the following implicit relation:

$$E_0 = E_s[1 - i\eta(I_s - \theta)] \quad \text{with} \quad I_s \equiv |E_s|^2. \quad (2.2)$$

Rewriting in terms of the input I_0 ($I_0 \equiv |E_0|^2$) and output I_s intensities:

$$I_0 = I_s[1 + \eta^2(I_s - \theta)^2] = I_s[1 + (I_s - \theta)^2] \quad (2.3)$$

where we see that the cavity is bistable for $\theta > \sqrt{3}$ independently of the parameter η (the sign of the nonlinearity). This bistability is shown in Fig. 2.1.

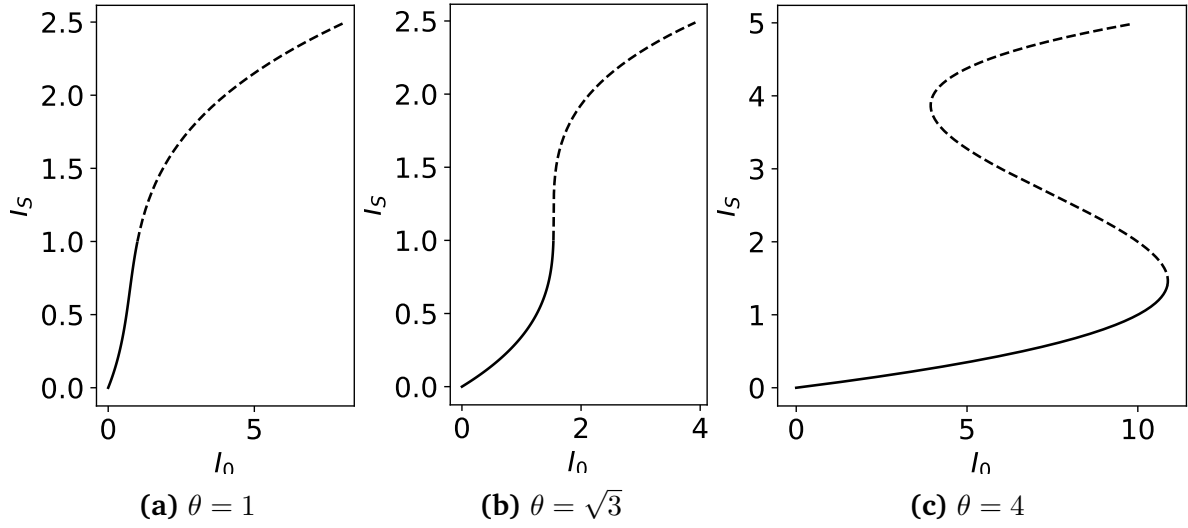


Figure 2.1: Bistability threshold of the homogeneous solution: Intensity of the homogeneous solution I_s as a function of the input intensity I_0 for a self-focusing Kerr cavity varying the value of the detuning. Solid and dashed lines indicate stable and unstable solutions, respectively.

2.1 Linear stability analysis

We perform now a linear stability analysis of the homogeneous solution in the self-focusing case ($\eta = +1$) with respect to spatially periodic perturbations. From this analysis we expect to obtain a range of values where a self-organized pattern emerges. The dispersion relation obtained from the analysis is:

$$\lambda(\vec{k}) = -1 \pm \sqrt{-(\theta + k^2 - 3I_s)(\theta + k^2 - I_s)} \quad (2.4)$$

where $\lambda(\vec{k})$ is the linear growth rate of a perturbation with a wavevector \vec{k} (with modulus $k = |\vec{k}|$). This equation allows us to determine the stability of the solutions in Fig. 2.1.

For $\theta < \sqrt{3}$ (Fig. 2.1a), the homogeneous solution is monostable. In this case, a pattern forming instability takes place at a critical value $I_s = I_c = 1$ with corresponding wavenumber $k_c = \sqrt{2 - \theta}$. I_s can now be used as a proper control parameter. For values of the pump intensity above threshold I_c , the maximum linear growthrate is for wavevectors with modulus:

$$k_{\max} = \sqrt{2I_s - \theta}. \quad (2.5)$$

At threshold $I_s = 1$, $k_{\max} = k_c$. As the physical values of k_{\max} are real, this equation is valid only for $\theta < 2$. The value of k_{\max} comes from a balance between the diffractive phase

modulation k_{\max}^2 , the nonlinear phase modulation $2I_s$, and the cavity detuning θ .

If we increase the detuning to $\theta = \sqrt{3}$, the homogeneous solution has a cusp. This is shown as a curvature change at Fig. 2.1b. For $\theta > \sqrt{3}$, the upper branch is always unstable. Regarding the lower branch, if $\theta < 2$ is unstable with respect to finite wavenumber perturbations for pump intensities above threshold I_c , while for $\theta > 2$, the lower branch homogeneous solution is stable until the fold (Fig. 2.1c).

For the self-defocusing case ($\eta = -1$), the pattern forming instability exists only for $\theta > 2$. But, since the upper branch is always stable, the pattern instability is frustrated by the bistable switching [11]. Therefore, no pattern solution emerges.

In order to obtain an hexagonal pattern solution, we work in the self-focusing case outside the bistable regime $\theta < \sqrt{3}$ ($\theta = 1.0$ and $\eta = +1$).

2.2 Hexagonal patterns

For the system considered, a nonlinear analysis predicts the emergence of an hexagonal pattern [11]. This is related to the existence of quadratic nonlinearities in the equation for the perturbed homogeneous solution. Note that, if we rewrite the Eq. (2.1) with $E(\vec{x}, t) = E_s(1 + A(\vec{x}, t))$, we obtain:

$$\begin{aligned} \partial_t A &= - [1 + i(\theta - |E_s|^2)] A + i\nabla^2 A + i|E_s|^2 (A + A^* + A^2 + 2|A|^2 + |A|^2 A) \\ &= - [1 + i(\theta - I_s)] A + i\nabla^2 A + iI_s (A + A^* + A^2 + 2|A|^2 + |A|^2 A) \end{aligned} \quad (2.6)$$

The transition is subcritical. Therefore, once the hexagonal pattern is formed, is stable for a range of values of I_s bellow threshold. Due to secondary instabilities of the stationary patterns, the hexagons may appear oscillating. The amplitude of this oscillation decreases until the hexagons become stationary. Moreover, due to the subcritical character of the transition, even at threshold hexagons have a significant amplitude. Therefore, we have to consider the six fundamental wavevector and a finite number of their harmonics in our analysis, as they have significant intensity.

In general, we write the stationary hexagonal pattern solution as:

$$E_h(\vec{x}) = \sum_{n=0}^{N-1} a_n e^{i\vec{k}_n^0 \vec{x}} \quad (2.7)$$

where \vec{k}_n^0 are the wavevectors of the pattern (the ones corresponding with the peaks in Fig.2.2¹), a_n are the complex amplitudes of this wavevectors and N the number of Fourier

¹From a numerical simulation performed on a 2048 x 2048 grid with periodic boundary conditions and discretization $\Delta k_y = k_0/16$ and $\Delta k_x = k_0 \sin(\frac{\pi}{3})/16$, to fit exactly the hexagonal pattern in Fourier space.

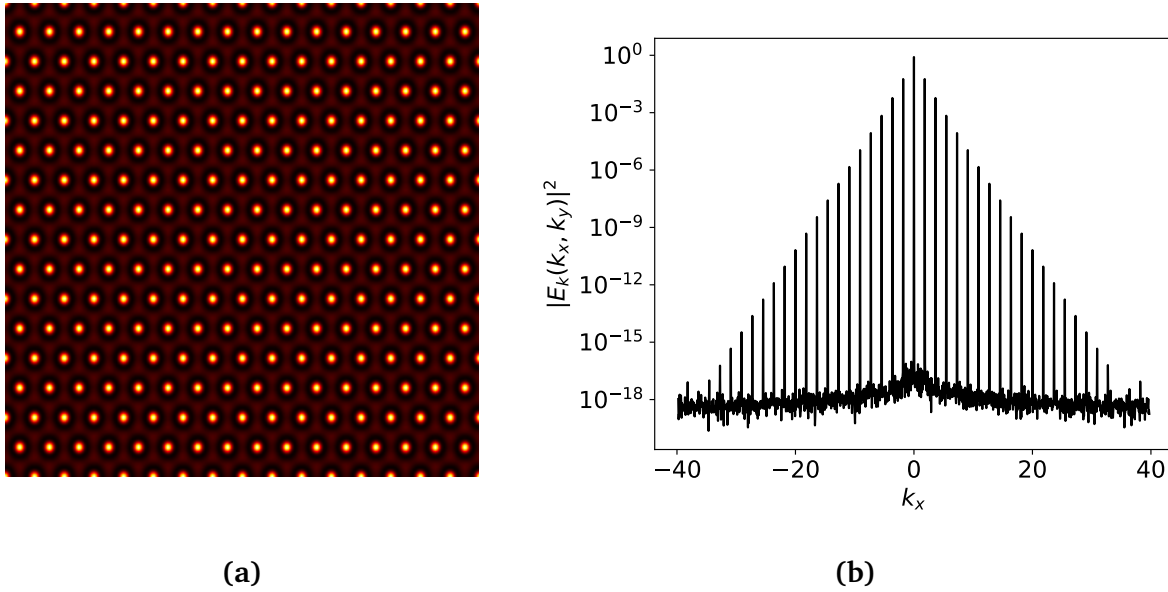


Figure 2.2: Stationary hexagonal pattern solution (a) $|E(x, y)|$ representation with $\vec{x} = (x, y)$. Bright (dark) colour indicates high (low) values of $|E(x, y)|$. **(b)** Cross section along the k_x axis of the power spectrum (far field) $|E_k(k_x, k_y)|$.

modes considered in the analysis. We consider \vec{k}_0^0 the homogeneous mode and the other $n = 1, N - 1$ are the six fundamental wavevectors and their harmonics, ordered by the absolute value of the complex amplitude. In our analysis, the coefficients a_n are obtained from numerical simulations.

The region of existence of stationary hexagonal patterns in our system has been previously studied in [9] (Fig. 2.3²) in more detail. Notice that, for every value of I_s above the critical value I_c , a range of hexagonal solutions with different wavenumber k become possible. Below this threshold, as hexagons are subcritical, they exist with a smaller intensity until the lower limit (grey solid line in Fig. 2.3) where there is a saddle-node bifurcation. This comes from the collision between the stable hexagonal pattern branch and the unstable one that starts from the homogeneous solution at point where $\lambda(k) = 0$. For our perturbation propagation analysis, this subcritical range is not suitable because a localized perturbation in a subcritical hexagonal can drive our system to the homogeneous solution. Thus, the analogy with a solid would not be valid. Therefore, we need to place system above the marginal stability curve of the homogeneous solution (black line in Fig.2.3).

²Note that this marginal stability diagram is computed by solving equation:

$$\partial_t E = -(1 + i\eta\theta)E + i\nabla^2 E + E_0 + i\eta\alpha|E|^2 E$$

where $\alpha = 2$. Our case corresponds with $\alpha = 1$. Therefore, our values of the pump intensity I_s are twice the values in this representation.

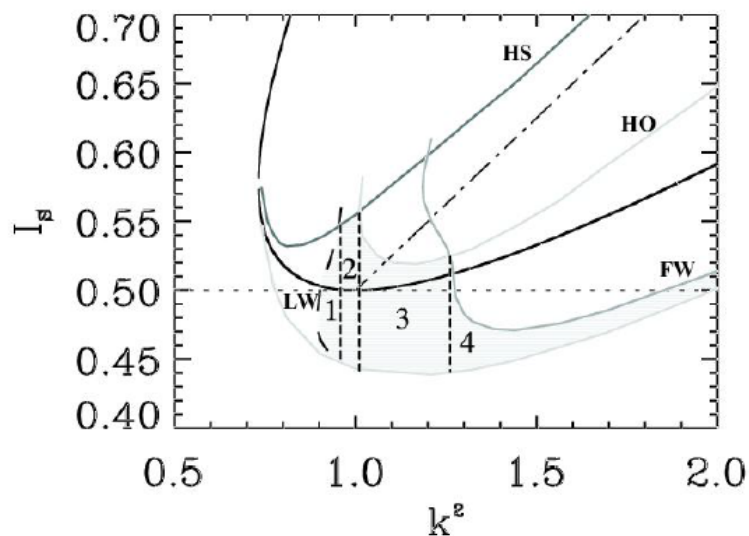


Figure 2.3: Marginal stability diagram of the hexagonal pattern solutions. Shaded region shows where the stationary hexagonal patterns are stable. Each enumerated sub-region correspond to hexagonal patterns that undergo different instabilities, where the intensity pumped the system out the stable region. From Ref. [9]

2.3 Secondary bifurcations of stationary hexagonal patterns

We perform a linear stability analysis of the stationary hexagonal solutions in order to determine their stability as a function of the input power. The method used is the same as in Ref. [9]. As we have a general expression of the hexagonal pattern in terms of the complex amplitudes of the Fourier modes, Eq. (2.7), we can linearise around this stationary solution $E(\vec{x}, t) = E_h(\vec{x}) + \delta E(\vec{x}, t)$ and get an equation for the perturbations:

$$\partial_t \delta E = -(1 + i\theta)\delta E + i\nabla^2 \delta E + i [2|E_h|^2 \delta E + E_h E_h \delta E^*] \quad (2.8)$$

This equation results in a eigenvalue problem $\partial_t E(\vec{x}, t) = L(E_h)\delta E(\vec{x}, t)$ where the coefficients of L are periodic. Therefore, according to Bloch theorem, our solution can be written as a superposition of Bloch waves (see Appendix B for more information). Thus, from Eq. (2.8), we obtain a set of linear equations for the complex amplitudes $\delta a_n(\vec{q}, t)$ corresponding with the Fourier modes with wavevector $k_n^0 + \vec{q}$:

$$\begin{aligned} \partial_t \delta a_n(\pm\vec{q}) &= \left[-(1 + i\theta) - i|k_n^0 \pm \vec{q}|^2 \right] \delta a_n(\pm\vec{q}) \\ &+ i \left[2 \sum_{l=0}^{N-1} \sum_{m=0}^{N-1} a_l a_m^* \delta a_{n-l+m}(\pm\vec{q}) + \sum_{l=0}^{N-1} \sum_{m=0}^{N-1} a_l a_m \delta a_{-n+l+m}(\mp\vec{q}) \right] \end{aligned} \quad (2.9)$$

where $\delta a_{n-l+m}(\pm\vec{q}) = \delta a_j(\pm\vec{q})$ with index j corresponding with $k_j^0 = k_n^0 - k_l^0 + k_m^0$. If we consider the vector $\vec{\Sigma}(\vec{q}, t) = (\delta a_1(\vec{q}, t), \dots, \delta a_N(\vec{q}, t), \delta a_1^*(-\vec{q}, t), \dots, \delta a_N^*(-\vec{q}, t))$, we can rewrite equation (2.9) as an eigenvalue problem:

$$\partial_t \vec{\Sigma}(\vec{q}, t) = M(a_n, \vec{q}) \vec{\Sigma}(\vec{q}, t). \quad (2.10)$$

Solving it, we obtain $2N$ eigenvalues $\lambda_n(\vec{q})$ ($n = 0, \dots, 2N - 1$) from matrix $M(a_n, \vec{q})$, and their corresponding eigenvectors $\vec{\Sigma}_n(\vec{q}, t)$. These eigenvalues determine the stability of the hexagonal pattern solution against periodic perturbations containing any set of wavevectors $k_n^0 \pm \vec{q}$. In order to discuss the role of each eigenvalue that drives the system to the different instabilities, we order the eigenvalues according to their real part $\Re[\lambda_n(\vec{q})] \geq \Re[\lambda_{n+1}(\vec{q})]$.

This analysis result is shown in Fig. 2.3 and is the reason why the shadowed region, where the hexagonal pattern is stable, does not cover all the $I_s - k^2$ space above the saddle-node line (lower grey line). Lines LW (long-wavelength), HS (homogeneous stationary), HO (homogeneous oscillatory) and FW (finite-wavelength) indicate the different types of secondary instabilities that hexagonal patterns can exhibit. The points where two instability lines cross is called a co-dimension two bifurcation point.

For our problem, we need the hexagonal pattern solution to be stable, above the marginal stability curve of the homogeneous solution and not undergoing any new instability. According to Fig. 2.3, this force us to place our system to the upper part of regions 1, 2 or 3. Depending on the region, the dynamics of the system while going to the stable solution are different because the system is close to a new instability line. Therefore, we discuss now briefly every type of instability following the analysis performed at Ref. [9] to choose the most suitable situation for our perturbation propagation.

Long-wavelength instability (region 1)

For this case, hexagons become unstable against long-wavelength perturbations ($\vec{q} \approx \vec{0}$) when pump is increased above LW instability line (dashed in Fig.2.3). This instability is associated to the family of hexagonal patterns solutions possible due to the translational invariance (phase instability). This is an effect of the 2 first branches $\lambda_{0,1}(\vec{q})$ of eigenvalues that correspond to the neutrally stable eigenmodes result of the translational invariance, in other words, the Goldstone modes. In fact, the Goldstone mode is for $\vec{q} = \vec{0}$, and the branches emerging from it for the values of $\vec{q} \neq \vec{0}$ are called soft modes.

Following a numerical simulation, we can see how an hexagonal pattern of a certain wavevector k for I_s above LW instability become unstable and the pattern is replaced for another with a larger value of k .

Homogeneous stationary instability (region 2)

This instability is characterized by a different branch $\lambda_i(\vec{q})$, which is parabolic around $\vec{q} = \vec{0}$, and whose maximum $\lambda_i(\vec{0})$ goes from negative to positive as we increase pump intensity.

In this case, $\lambda_i(\vec{0})$ is a branch of real eigenmodes. When the pump intensity is increased above HS instability line (dark grey in Fig. 2.3), the hexagonal patterns undergo a stationary bifurcation. As a result, a new shifted hexagonal lattice appears in the near-field.

Homogeneous oscillatory instability (region 3)

As the previous instability, this one is also characterized by a branch $\lambda_i(\vec{q})$ as in the previous case. Although, now the eigenvalues are complex. In fact, there are two branches that are complex conjugates. The maximum of their real part becomes positive when increasing I_s above the HO instability line (the above grey one in Fig.2.3). The corresponding imaginary part is different from 0. Therefore, the hexagonal pattern starts to oscillate homogeneously with an angular frequency $\omega = \Im[\lambda_i(\vec{0})]$.

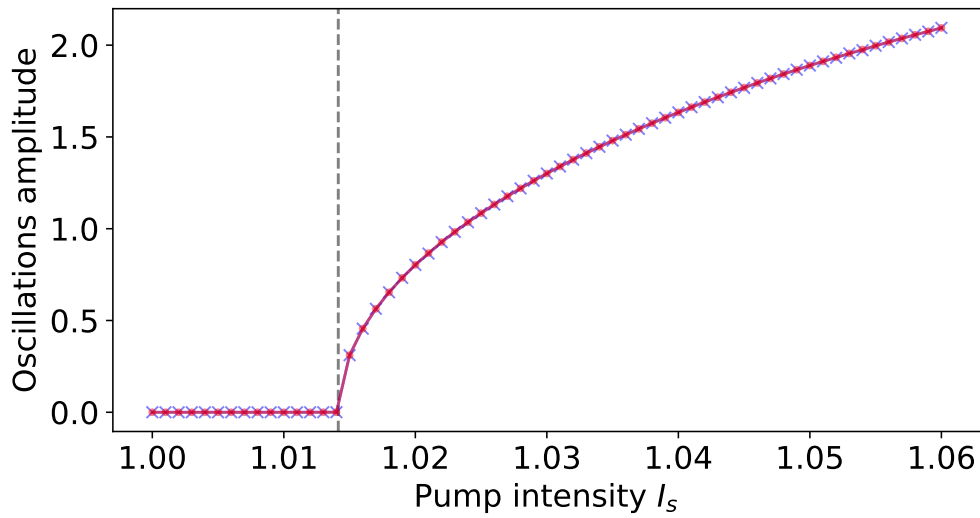
In other words, the hexagonal pattern peaks undergo a Hopf bifurcation. If we consider one peak isolated (Kerr Cavity Soliton), this would also exhibit a Hopf bifurcation [9]. Therefore, this gives rise to considering the pattern as a collection of independent coupled oscillators.

To study the propagation of oscillating waves in a pattern, we need to place our system in region 3 above the marginal stability curve of the homogeneous solution and as close as possible to the HO instability. This must be done because with the Hopf eigenmodes with real part negative close to 0, the perturbation will excite this modes what is expected to lead the perturbation to propagate faster along the hexagonal peaks of the pattern. Therefore, we analyse in detail the dynamics around this instability.

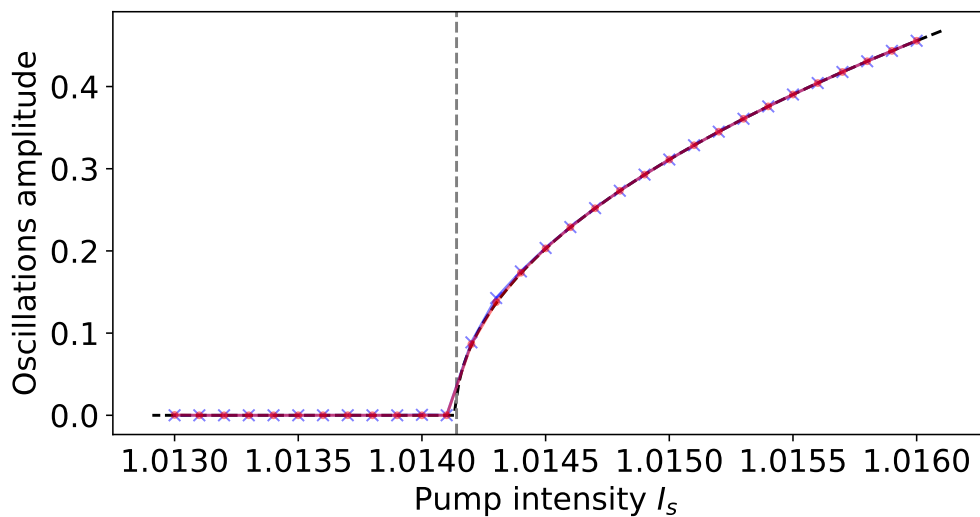
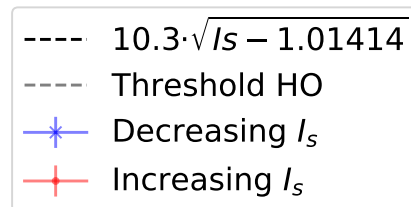
First of all, we perform numerical simulations in a small system of 256×256^3 with an hexagonal pattern with $k_0 = 1.05$ as an initial condition. Increasing and decreasing I_s , we can compute the oscillation amplitude (Fig. 2.4). In this representation, the amplitude of the oscillations is computed as an average over 40000 units of time (that include an important amount of oscillations) when the oscillation amplitude is already stable (very long trajectories). Statistical errors are included but the values can not be appreciated.

The first interesting result is that we get the same oscillations amplitude for both increasing and decreasing the pump. Therefore, there is no hysteresis from the system to keep oscillating and so, the Hopf bifurcation is supercritical.

³With periodic boundary conditions and Fourier discretization defined by $\Delta k_y = k_0/2$ and $\Delta k_x = k_0 \sin\left(\frac{\pi}{3}\right)/3$, to fit exactly the hexagonal pattern in Fourier space.



(a)



(b)

Figure 2.4: Amplitude of oscillations of a peak as a function the pumped intensity I_s (a) and zoom around the instability threshold (b). The red (blue) line representation corresponds with the results increasing (decreasing) the pump intensity. The vertical dashed grey line represents the HO instability threshold. The black dashed line in the zoom plot is the result of a curve fit.

This supercritical behaviour indicates that, when we cross the threshold very slowly from higher I_s , the oscillations amplitude decreases to very small values until the threshold, where the amplitude is null. On the other hand, from lower values of I_s , the system goes to the stable hexagonal pattern solution oscillating because of the presence of complex conjugate eigenvalues not very damped with a imaginary part different than 0. Therefore, approaching threshold results in a slower relaxation of the amplitude at each step and, as a consequence, we need longer and longer trajectories to get the stable solution. From Fig. 2.4b, we can determine graphically the oscillatory instability threshold as the last value with null oscillations amplitude, which error comes from the I_s step chosen:

$$I_{\text{HO}}^{\text{graph}} = 1.0141 \pm 0.0001 \quad (2.11)$$

In addition, we also study the amplitude behaviour. As it is a Hopf bifurcation, from dynamical systems theory [12], one expects a square root dependence with the order parameter. We verified this information with a curve fit that gives additional information about the threshold. Our function chosen to fit the data is:

$$A(I_s) = a(I_s - I_{\text{th}})^b \quad (2.12)$$

where a , b and I_{th} are parameters to fit with the data. The result of this curve fit is shown in Table. 2.1.

Table 2.1: Results from the fit shown at Fig. 2.4.

a	b	I_{th}
10.290 ± 0.002	0.4959 ± 0.0001	1.014136 ± 0.000001

As we see, parameter $b \approx \frac{1}{2}$, what agrees with a Hopf bifurcation. Also, the threshold that the fit predicts is in agreement with the graphically obtained one but with a better precision. From all this analysis we can conclude that, in order to have a perturbation propagating long distances, we must place the system as close as possible to the Hopf bifurcation. In other words, the real part of the eigenvalues branch $\lambda_i(\vec{q})$ must be as close to 0 as possible (from the negative side) to help to sustain the propagation along the hexagonal peaks.

Considering a pattern with wavenumber $k_0 = 1.05$ as the one previously studied, we can choose a pump intensity of $I_s = 1.0141$ (slightly below threshold). Performing a numerical simulation, the hexagonal pattern is stable but the system initially oscillates homogeneously but finally evolves slowly to this solution (Fig. 2.5a and 2.5b⁴).

⁴System defined by a grid of 1024 X 1024 with Fourier discretization of $\Delta k_y = k_0/8$ and $\Delta k_x = k_0 \sin\left(\frac{\pi}{3}\right)/8$.

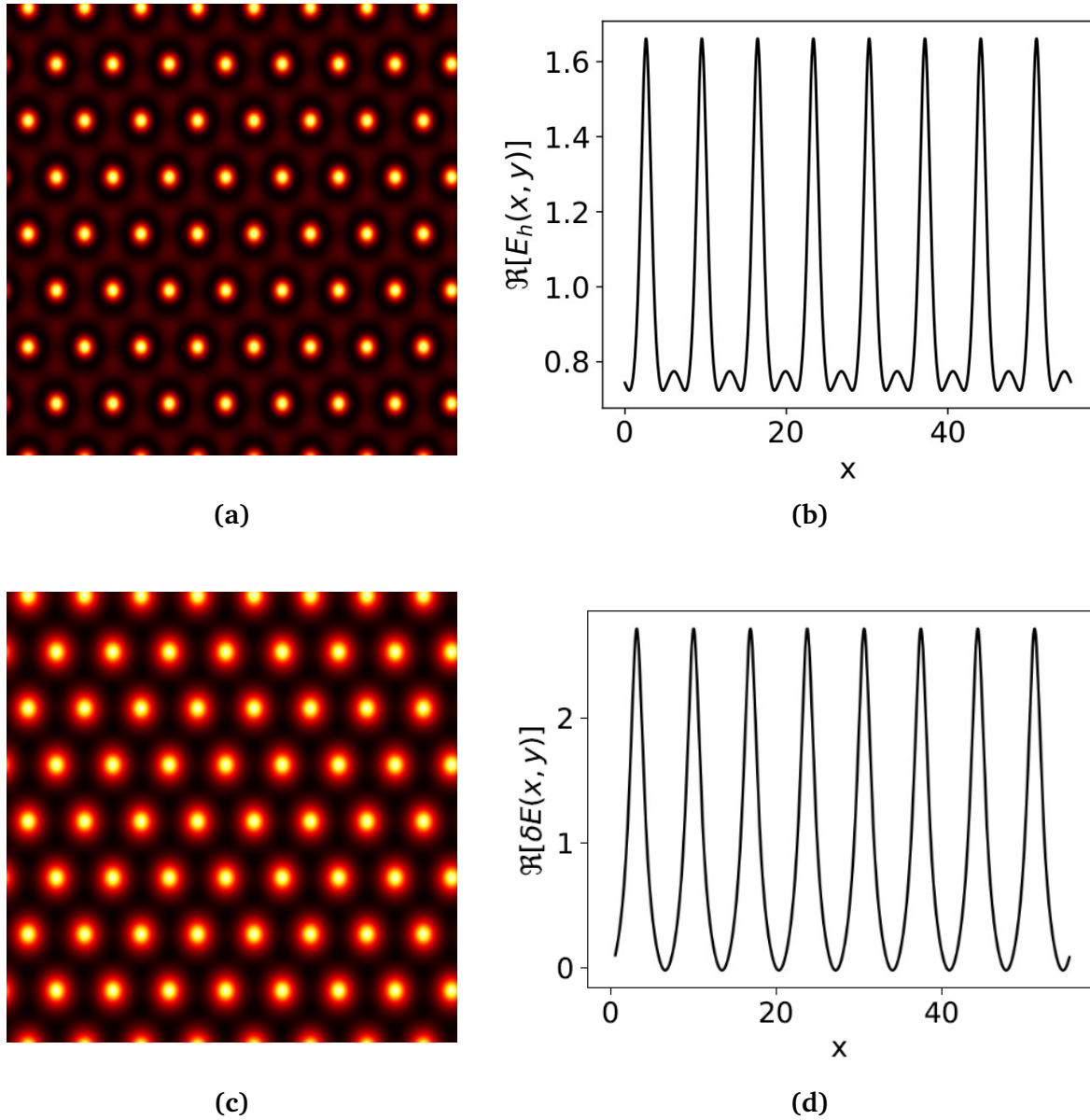


Figure 2.5: Hexagonal pattern and oscillatory mode representation at $I_s = 1.0141$. 2D representation of the hexagonal stable pattern $\Re[E_h(x, y)]$ **(a)** and the first unstable eigenmode corresponding $\Re[\delta E(x, y)]$ **(c)** as a function of $\vec{x} = (x, y)$. Transverse cut along the x direction at the center of the system of both, the pattern **(b)** and the mode **(d)**

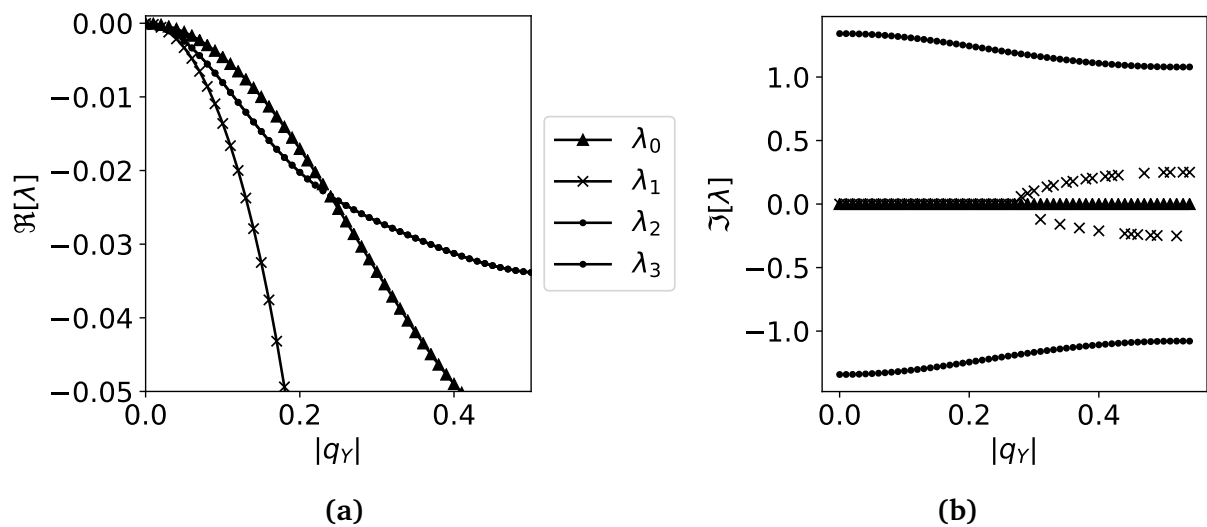


Figure 2.6: Eigenvalues representation for $I_s = 1.0141$. Real (a) and imaginary (b) part of the eigenvalues $\lambda(\vec{q})$ along a transverse cut in the q_y axis showing the 4 first branches (with higher $\Re[\lambda(q_x, q_y)]$ and ordered according this value at $\vec{q} = 0$.)

With the final result of this simulation, we use the complex amplitudes to make a linear stability analysis of this hexagonal pattern solution and get, from it, the eigenvalues and eigenvectors. Therefore, we can reconstruct the form of a perturbation due to the Hopf instability for the eigenvalue with higher real part $\lambda_{HO}(\vec{q} = \vec{0})$ (Fig. 2.5c and 2.5d). From this figure, we observe that this mode has approximately the same shape as the hexagonal pattern. This agrees with the idea of uniform oscillations. From the transverse cut (Fig. 2.5b and 2.5d) we observe that the oscillation is restricted to the hexagonal peaks, leaving the background unaltered.

We recall that, for this value of the pump intensity, the oscillatory solution with the mode previously represented is damped but with a $\Re[\lambda_{HO}(\vec{0})] \approx 0$. In Fig 2.6, we see the 4 branches, the 2 corresponding to the soft modes ($\lambda_{0,1}(\vec{q})$) and the 2 complex conjugate branches of the HO instability ($\lambda_{2,3}(\vec{q})$). Their real part meet approximately at $\Re[\lambda] = 0$ and exhibit a parabolic behaviour around $q_y = 0$. If we zoom enough, we see how the branches $\lambda_{2,3}(\vec{q})$ have a real part of the eigenvalues at $q_y = 0$ of ≈ -0.0002 while the for the Goldstone mode is of order 10^{-6} . Therefore, this mode is damped (allowing for the system to reach the stable solution) but not highly damped (what helps the perturbation propagation along the peaks).

In Fig. 2.6b we see that the imaginary part of the eigenvalues corresponding to the Hopf exhibits a parabolic behaviour around $q_y = 0$ starting at a value $\Im[\lambda_{HO}(\vec{0})] \neq 0$. Therefore, the mode previously represented at Fig. 2.5c and 2.5d oscillates with a frequency $\omega_{HO} = \Im[\lambda_{HO}(\vec{0})] \simeq 1.34$.

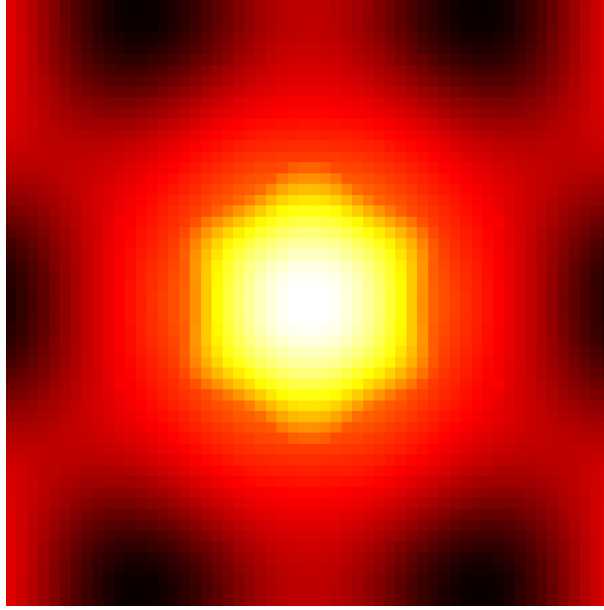


Figure 2.7: $\Re[\lambda_0(\vec{q})]$ as a function of the vector $\vec{q} = (q_x, q_y)$ for $I_s = 1.0141$. The center corresponds to a Goldstone mode $\Re[\lambda_0(0, 0)] = 0$. Dark (bright) colors indicates low (high) values of $\Re[\lambda_0(\vec{q})]$.

In Fig. 2.7, we see that the eigenvalues preserve the symmetry of the pattern. In addition, to compute the stability against any possible perturbation is enough to consider the \vec{q} inside the first Brillouin zone of the lattice defined by the wavevectors \vec{k}_n^0 of the pattern (shown in 2.7). Any perturbation with a vector \vec{q}' outside the first Brillouin zone is equivalent to other inside $\vec{q}' + \vec{k}_n^0$.

Chapter 3

Perturbation propagation

3.1 Characterization of the perturbation

In this chapter, we report the results of a numerical simulation with an hexagonal pattern with $k = 1.014$ at $I_s = 1.0141$ as initial condition, which is a stable solution for those parameters. This pattern is modified with a localized perturbation in one of the peaks of the hexagons. First of all, we explain why we choose this type of localized perturbation.

As the hexagonal pattern peaks have the shape previously reported at Fig. 2.5, the best way to produce a perturbation without causing any anisotropy is to consider a 2D Gaussian perturbation. This is chosen to have a width less or equal than the disturbed peak (see Fig. 3.1). The Gaussian profile is symmetrical if its amplitude in both directions x and y is the same ($\sigma_x = \sigma_y = \sigma$). Note that, depending on the value of amplitude σ , this kind of perturbation can have a width smaller than the characteristic wavelength of the hexagonal pattern. Therefore, it is not simple to predict its behaviour theoretically because we should not use approximations for long-wavelength perturbations.

In addition, as the perturbation is Gaussian, σ is a measure of the perturbation intensity (the smaller the σ , the higher the intensity). As we see in Fig. 3.1b, for $\sigma = 1$, the perturbation is small in comparison with the pattern amplitude. This allows us to use a linear analysis of the perturbation evolution. Nevertheless, in next section we see that this small perturbation is enough to excite a lot of interesting modes from the HO branch.

3.2 Numerical results

The main result of this section is the evolution of the system due to the initial perturbation (with $\sigma = 1$) computed numerically with the method described in Appendix A. To have a realistic scenario, we need to take a large system with an accurate discretization allowing the system to excite as much modes from the Hopf branch as possible. Therefore, we choose a system with the same characteristics as the one in Fig. 2.2 and we place an initial

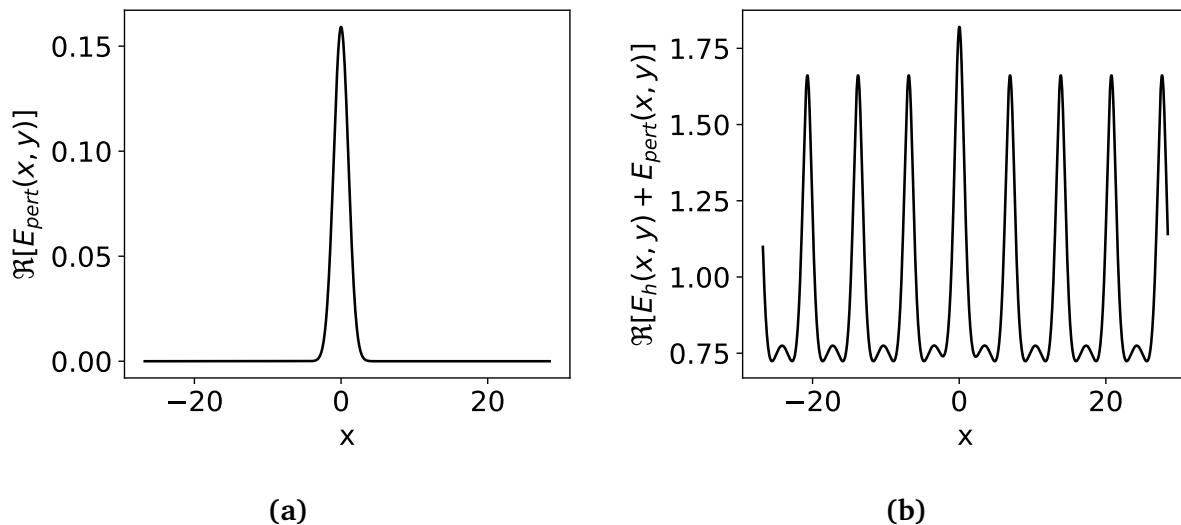


Figure 3.1: Perturbation representation. Transverse cut along x direction of the Gaussian perturbation itself (a) and compared with the hexagonal stable pattern (b). System characteristics as in Fig. 2.5.

Gaussian perturbation at the central peak of the system. The results of this evolution are shown at Fig. 3.2 and 3.3.

Fig. 3.2 shows the central peak intensity evolution in time. Initially we see how the perturbation excites an oscillating behaviour with a large amplitude that decreases with time. In this time, the system exhibits the propagation of the perturbation and the dynamics of this peak are driven by the excited modes, which decay according to their eigenvalues. This happens until $t \approx 45$, where we see a sudden change of period and amplitude. This indicates the moment when the uniform homogeneous oscillation prevails. From now on, the peak will continue oscillating with constant ω_{HO} (which coincides with the prediction $\Im\lambda_{HO}[\vec{0}]$). When all peaks in the pattern exhibit this transition, the system evolves following an homogeneous oscillation with a decreasing amplitude until the stable state is reached.

Now let's analyse the behaviour of the whole pattern. In the early stages of the simulation (Fig. 3.3a) one can appreciate a circular front of the perturbation propagating through the background. Notice that Fig. 3.3 shows the evolution of the difference between the field and the stable hexagonal pattern solution. As expected, this perturbation is very damped and rapidly becomes inappreciable. This is because modes involving very small wavelength (large wavevector modulus k) are very damped. Being close to the HO bifurcation does not affect significantly to background dynamics because, as we see in Fig. 2.5, the first unstable mode for the Hopf just affects the peaks from the hexagonal pattern.

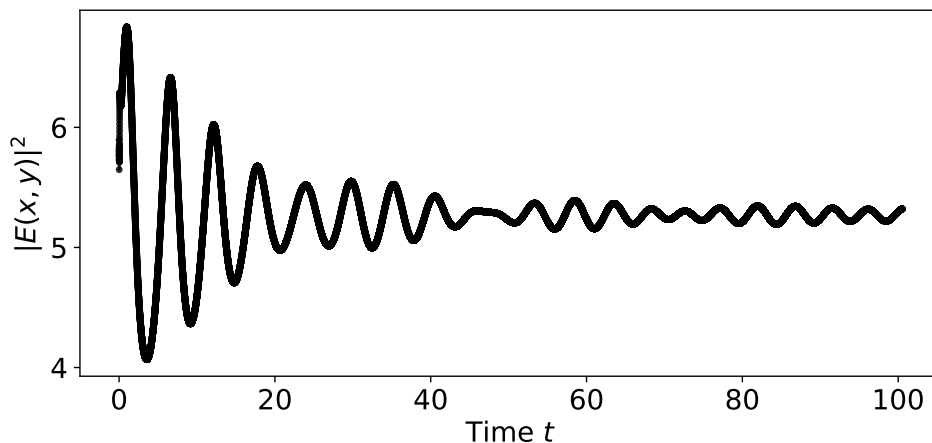


Figure 3.2: Time evolution of the central peak of the hexagonal pattern in Fig.3.3.

As time evolves, the central peak starts to oscillate creating a front that gets to the first neighbours and, at the same time, all hexagonal peaks start to oscillate homogeneously with an amplitude that decreases with time, because the system tends to the fixed point (stable hexagonal pattern). Therefore, we have two dynamical regimes coexisting: the excitation of different modes at the center of the system and the homogeneous oscillation at peaks where the perturbation propagation has not reached yet. This can be seen in Fig. 3.3b, where we see how the central peak and its nearest neighbours have an intensity much low than from the rest of the pattern. The interesting point here is also that, as the perturbation propagation reaches a ring of neighbours, one can see how also the soft modes are excited (these modes are characterized by the presence of a dark and bright part side by side at the hexagonal pattern peaks). This is because the perturbation is causing a deformation of the hexagons that is rapidly recovered (see first neighbours in Fig. 3.3b).

In the following representations (Fig. 3.3c, 3.3d and 3.3e) we see how this perturbation expands and reaches the 2nd, 4th and 7th ring of neighbours, respectively. This happens while all hexagons are excited by the homogeneous oscillation mode. In addition, in this representation one can see the excitation of other modes like the anti-synchronous oscillation between peaks in consecutive rings. In Fig. 3.3d, we see how the first ring of neighbours has a low amplitude, the second one has a higher one, the third has it low again and the fourth is the highest, as the front is reaching it. Notice also that this front velocity is similar in both directions, \vec{x} and \vec{y} , predicting a circular propagation of the perturbation.

As the system is dissipative, the perturbation propagation does not conserve its initial intensity and, after an amount of time, is not appreciable anymore. This is also because the modes that excite this behaviour are damped and the system tends to the stable solution. Therefore, in the last evolution image (Fig. 3.3f) we see the pattern oscillating at

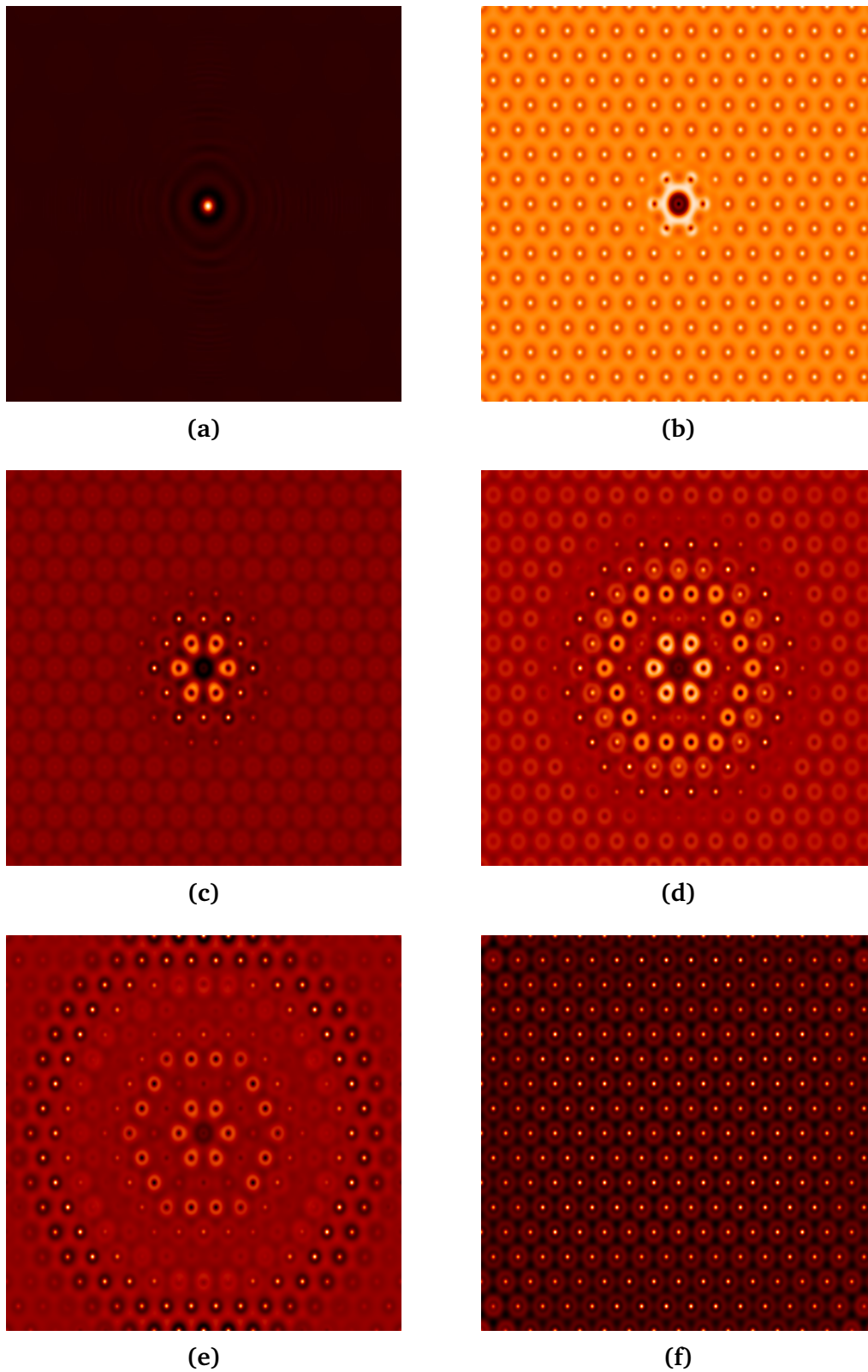


Figure 3.3: Time evolution of the field $|E(x, y) - E_h(x, y)|$ of a system with an initial wavenumber $k = 1.014$ and pump intensity $I_s = 1.0141$. Each image is taken at $t = 0.5$, (a) 8, (b) 19.5, (c) 42.5, (d) 65.5 (e) and 99,5 (f) units of time. The representation in (a) is a zoom to the center of the system, in order to see the background waves. The time step, following the integration method in Appendix A, is $2\delta t = 2 \cdot 10^{-3}$.

constant frequency with an homogeneous amplitude that decreases with time. For enough amount of time, the amplitude becomes null and we recover the initial state of the system.

Velocity of the perturbation propagation

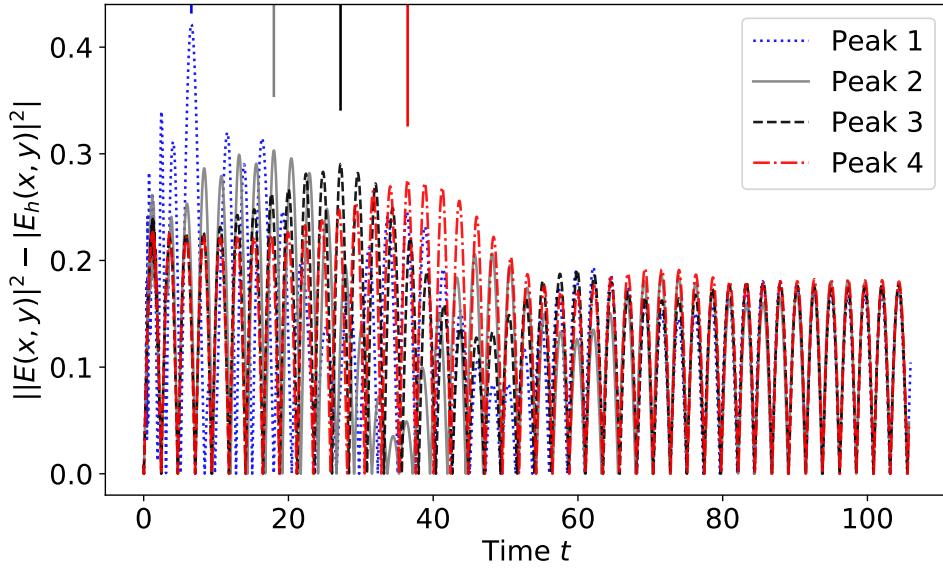
To study the velocity of the wavefront of the propagation, we need to consider a larger perturbation. This allows us to detect where is the front for longer time (when the perturbation is highly dissipated). Therefore, we consider $\sigma = 0.2$, which can still be considered a small enough perturbation to be predicted by linear stability analysis.

To calculate the velocity we analyse the time evolution (as in Fig. 3.2) for the nearest peaks to the centered (perturbed) one along the x and along the y-axis. Therefore, at each representation of the evolution, we must see a maximum value when the perturbation arrives to the peak. From the differences of time where this maximum takes place we obtain the velocity of the wave. Thus, this analysis has 2 limitations: the dissipation of the perturbation, because if the wave front does not get one of the considered peaks we get no information from it (attempted to solve with a higher perturbation), and the size of the system, because the larger the system, the higher the number of peaks in it to analyse. Therefore, we increase the size to a system defined by a grid of 4096 X 4096 with a Fourier discretization of $\Delta k_y = k_0/32$ and $\Delta k_x = k_0 \sin\left(\frac{\pi}{3}\right)/32$ ($k_0 = 1.05$). Notice that increasing the grid size allows us to decrease the Fourier discretization intervals for the integration, what results in a increase of the discretization steps in real space and, as a consequence, an increase of the system size. The result of this analysis is in Fig. 3.4 and Table.3.1.

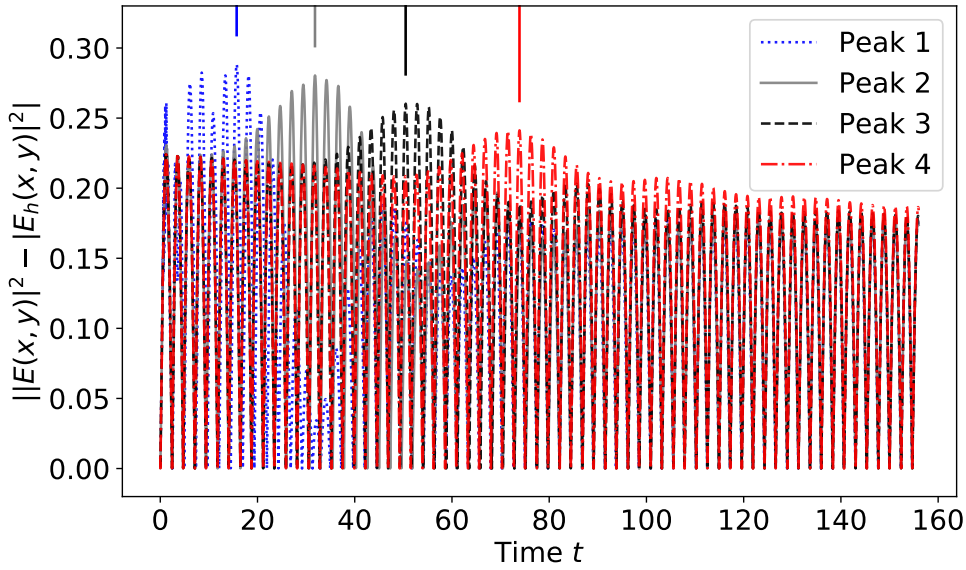
For the closest peaks to the disrupted one we see a behaviour as the one in Fig. 3.2, for this peak itself. An initial perturbation followed by the decaying of the intensity until the peak oscillates homogeneously with the rest. However, for the farthest ones, we see an initial homogeneous oscillation followed by a disruption that creates a maximum at certain moment until this peak recovers the same original oscillation. Therefore, this representation agrees with the results previously mentioned and gives new information about when and where is the wave front of the perturbation. Note here how the perturbation gets rapidly dissipated even being that close from the starting point of the perturbation.

From the vertical lines, we can see the time that takes for the perturbation to go from one peak to another is similar for all the peaks. Computing this time, we can also extract the velocity of the wave front, as the distance between peaks in the hexagonal pattern is always the same in each direction. This is a way to check if the propagation its really circular or not.

Looking to the table 3.1, notice that the distance between two consecutive peaks in the y direction is approximately twice the distance between two along the x direction. And, looking to the values of the time that takes for the perturbation to propagate between peaks, we see that happens the same. Therefore, by computing the velocity we check that the wave front propagates circularly.



(a)



(b)

Figure 3.4: Time evolution of the intensity difference $||E(x, y)|^2 - |E_h(x, y)|^2|$ of the nearest peaks to the central one in the x (a) and y (b) direction. The peaks numeration makes reference of the closeness to the central peak, from 1 to N_p (N_p the number of peaks considered). The top left vertical lines highlight the maximum of each trajectory for the corresponding peak, according to the color.

Table 3.1: Results extracted from Fig. 3.4 for the peaks along the x (a) and y (b) direction. For each peak i , we present the amount of time that took for the perturbation to reach it from the previous peak $i - 1$ and its velocity according to this time interval.

Peak i	1	2	3	4	5	6	7	8	9
$t_i - t_{i-1}$	6.596	11.398	9.216	9.268	14.052	9.306	14.052	9.334	14.056
v_x^i	1.05	0.61	0.75	0.75	0.49	0.74	0.49	0.74	0.49

(a)

Peak i	1	2	3	4	5	6	7
$t_i - t_{i-1}$	15.712	16.110	18.648	23.414	18.700	23.424	18.742
v_y^i	0.76	0.74	0.64	0.51	0.64	0.51	0.64

(b)

If the propagation is circular, v_x^i and v_y^i should have the same value. Nevertheless, we see discrepancy between the values corresponding to different peaks. This is because the peaks oscillate with a frequency faster than the perturbation modulation. Thus, the value of the time for the perturbation to reach the peak is constrained to the oscillation maximums and minimums, causing an error in this value. However, if we compute the average, with its corresponding statistical error, we obtain:

$$\bar{v}_x = 0.63 \pm 0.04 \quad \bar{v}_y = 0.64 \pm 0.04 \quad (3.1)$$

what reflects an agreement between the two directions, confirms the circular propagation and give us an estimation of how fast the perturbation propagates. Moreover, we do not see any dependence of the velocity with the distance to the perturbed peak. Therefore, it makes sense to assume that the velocity is constant until the perturbation is completely dissipated.

We need to mention that this velocity previously reported refers to how fast the initial perturbation expands through the system. Following solid-state theory, we see that the group velocity of the wave created by our perturbation is null:

$$v_g = \left. \frac{\partial \omega(q)}{\partial q} \right|_{q=0} = \left. \frac{\partial \Im[\lambda(q)]}{\partial q} \right|_{q=0} = 0 \quad (3.2)$$

This comes from the parabolic behaviour of the imaginary part of the eigenvalues around $q = 0$. Thus, the perturbation center does not travel through the system. This differs with a solid system, where the frequency is directly proportional to the wavevector in the long wavelength limit, what results in a velocity of sound independent of frequency.

3.3 Theoretical analysis

Interpreting the numerical result from chapter 3 is not simple, as we have system where the dynamics are the result of a balance between different elements: diffraction, dissipation, excitation of unstable modes... Therefore, we cannot simply use a wave solution in our equation and characterize it.

In order to replicate our results, first we need to see which are the important contributions that give rise to the perturbation propagation phenomena. In Fig. 3.3 we see that the propagation can be described, roughly, as a homogeneous oscillation of a self-organized pattern with a modulation of the amplitude that expands.

The homogeneous oscillation, as we have studied, is characterized by the imaginary part of the Hopf eigenvalues. By performing a linear stability analysis of the pattern solution we obtained this eigenvalues (Fig. 2.6). At our numerical simulation, we have the presence of different oscillations due to the excitation of different modes in this branch (for the different values of \vec{q}). To simplify this theoretical representation, we take just the one with higher real part, in other words, the first one that become unstable at threshold. Thus, the frequency $\omega_{HO} = \Im[\lambda_{HO}(\vec{q} = \vec{0})]$.

Regarding to the hexagonal pattern, note that what is represented in Fig. 3.3 is the difference between the field and the original stable pattern. Therefore, to model this, we can use the eigenvectors corresponding to the $\lambda_{HO}(\vec{q} = \vec{0})$ (as the one represented in Fig. 2.5c).

Thus, we just need to model the amplitude modulation to reply our results theoretically. If we assume that our perturbation has a long wavelength, we know that the slowly varying amplitude modulation close to a Hopf bifurcation is governed by the Complex Ginzburg-Landau Equation (CGLE) (3.3). Although this is not strictly speaking our case, because the perturbation is localized to a hexagonal pattern peak, we use this to get an approximation of the behaviour.

To derive the CGLE from equation (2.1) with a multiple scale analysis is complicated. Nevertheless, we can use this equation by setting the parameters according to their role to fit those of our system.

As we are bellow threshold, the base solution of the CGLE is the homogeneous one ($A(\vec{x}, t) = 0$). Therefore, the role of the nonlinear part is not significant and we can neglect it ($c = 0$).

$$\partial_t A(\vec{x}, t) = \mu A(\vec{x}, t) + (a + ib)\nabla^2 A(\vec{x}, t) + ic|A|^2 A(\vec{x}, t) \quad (3.3)$$

To place the system close to the Hopf we set the distance to threshold (from negative values) $\mu = -10^{-4}$.

The parameters a and b are related to the convexity of the Hopf eigenvalues branch close to $\vec{q} = \vec{0}$, and can be calculated from the linear stability analysis previously performed (Fig. 2.6):

$$a \simeq \partial_q^2(\Re[\lambda_{\text{Hopf}}]) \simeq 2 \quad b \simeq \partial_q^2(\Im[\lambda_{\text{Hopf}}]) \simeq 5.2 \quad (3.4)$$

With these parameters, we expect that a numerical integration, choosing as an initial state the perturbation used at previous section, should return us the amplitude modulation that we observe at the numerical integration. In addition, we must take into account that the dynamics of this equation are slowly varying with respect to our equation. However, we can extract a qualitative approximation for the numerical result with this 3 contributions together:

$$E'(\vec{x}, t) = A(\vec{x}, t)E_{\text{mode}}(\vec{x})e^{i\omega_{HO}t} + c.c \quad (3.5)$$

where $A(\vec{x}, t)$ is the modulation amplitude from the CGLE numerical integration, E_{mode} is the Hopf mode reconstructed from the eigenvectors and $e^{i\omega_{HO}t}$ is the oscillating term. Note that $E'(\vec{x}, t)$ is an approximation of the difference between the field solution and the stable hexagonal pattern $E(\vec{x}, t) - E_h(\vec{x})$.

The theoretical prediction results are represented in Fig. 3.5, where we see a similar evolution than in the numerical case. In Fig. 3.5a, we see the dissipation of the initial state starting. Now, as we do not have background dynamics, we can not see the highly damped wave propagating through it. As time increases we see how the perturbation propagates reaching the different rings of the hexagonal pattern (Fig. 3.5b and 3.5c). This is happening while the system oscillates homogeneously as in the numerical simulation. At this stage, the main difference with the numerical result is the missing modes getting excited and showing interesting phenomena (like soft modes). Finally, at Fig. 3.5d, we recover the same result as in the numerical simulation: an homogeneous oscillation with a frequency according to the first eigenvalue of the Hopf branch. This happens because the modulation of the amplitude gets dissipated and the term left is the oscillating one. Moreover, we should highlight that, because of the missing eigenmodes exciting the hexagonal pattern, this theoretical description does not predict the phase change when a peak is no more driven by the propagation effects and recovers the frequency corresponding to the homogeneous oscillatory mode (seen in Fig. 3.2).

If we perform a similar analysis regarding the velocity of the perturbation propagation, we get a prediction of the circular propagation and that the perturbation dissipates fast and rapidly becomes null (See Fig. 3.6). Note that this theoretical evolution gives a qualitative view of the perturbation propagation because we have not derived properly Eq. (3.3) from Eq. (2.1) with a multiple scale analysis. Therefore, we have no analytical expression to compare the results quantitatively. In addition, our perturbation is not suitable

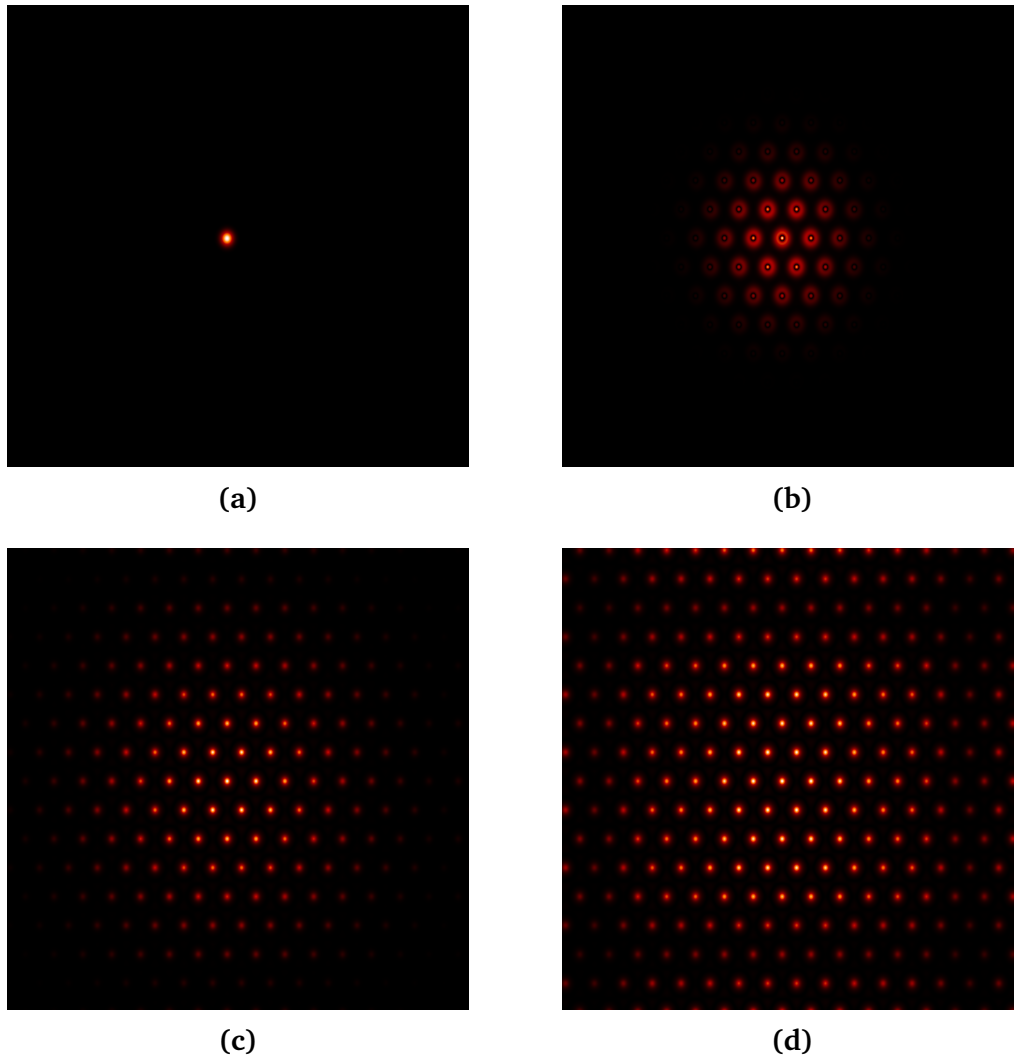
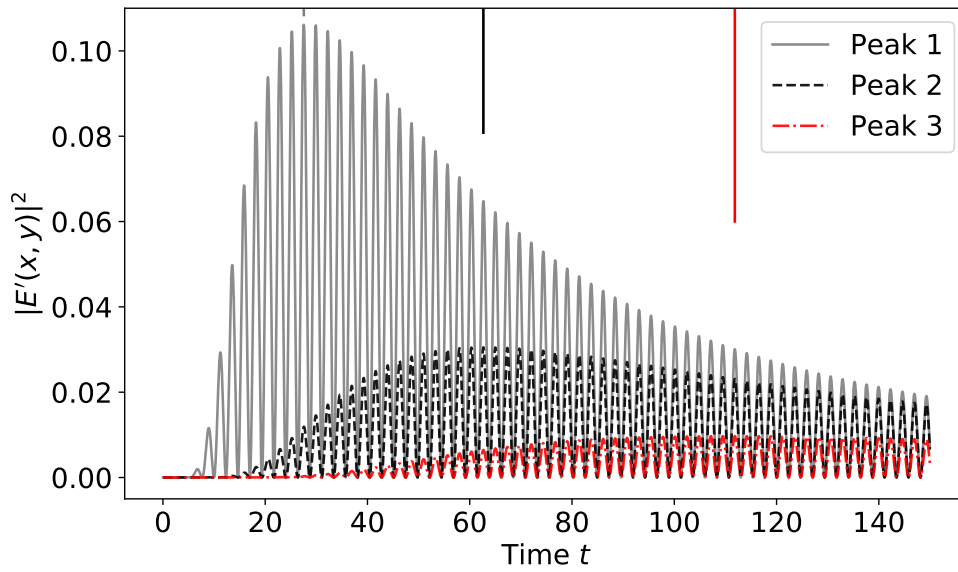


Figure 3.5: *Theoretical prediction for the time evolution of the field $|E'(x, y)|$ of a system with an initial wavenumber $k = 1.014$ and pump intensity $I_s = 1.0141$. Each image is taken at $t = 0.5$, (a) 3.5, (b) 11.5 (c) and 79 (d) units of time. The time step, following the integration method in Appendix A to compute the CGLE amplitude modulation is $\delta t = 10^{-3}$.*



(a)

Figure 3.6: *Time evolution of the intensity $|E'(x, y)|^2$ of the nearest peaks to the central one in y direction. The peaks numeration makes reference of the closeness to the central peak, from 1 to N_p (N_p the number of peaks considered). The top left vertical lines highlight the maximum of each trajectory for the corresponding peak, according to the color.*

to use CGLE as amplitude modulation because has initially short wavelength contributions. Nevertheless, as the contribution widens, the CGLE description is more suitable.

In addition, in Fig. 3.6, we see how the spacing between times t_i when the perturbation gets a peak is constant. This agrees also with the numerical results and suggests that, even though the intensity of the perturbation decreases, the velocity remains constant. For larger systems with higher values of the initial perturbation, this can be a very good tool of prediction of when and where a peak will increase its intensity.

Discussion and concluding remarks

In this thesis, we studied the perturbation propagation in self-organized patterns. We focused in optical patterns because of the motivation that recent experiments in this field can reproduce this phenomena. To carry out this study we used numerical simulations and amplitude equations to model this phenomena for a chosen differential equation as a case study, namely the Lugiato Lefever equation.

We started by characterizing the stability of the homogeneous solution and next, of the hexagonal pattern solution. From this analysis, we found the most suitable situation for our system to sustain a periodic perturbation. For a system with an important size, we performed a numerical integration of our equation for a perturbed pattern. We confirmed here the presence of a propagation along the peaks of the hexagons. We found that the perturbations propagation is highly dissipated and there is a moment when it becomes inappreciable. From this numerical results, we analyzed the characteristics of the perturbation propagation. From the velocity analysis, we confirmed that the propagation is circular and we gave an estimation of this value, which appears to be constant.

The main difference of our system with respect to a solid is that we found that group velocity is null for the long wavelength limit. Therefore, the energy transmission through the peaks is not net and we cannot assume our medium as a continuum for this limit.

Furthermore, we used a theoretical analysis based on the CGLE to give a qualitative description of the propagation perturbation and recover the numerical results. Nevertheless, this theoretical description misses interesting phenomena from numerical results due to the initial excitation of damped modes.

A further analysis on this work includes using higher values of the perturbation in larger systems in order to analyse better the perturbations evolution through the peaks. In addition, one can check the interaction between two perturbations propagation in the same system and how would affect to the oscillation of the rest of the pattern. Regarding to the theoretical description, an advanced work could face the challenge of getting the CGLE from the initial Lugiato-Lefever equation to get an analytical expression to compare with our numerical results.

The study of perturbation propagation in self-organized patterns, including cold atomic systems, could confirm experimentally the results presented in this work.

Appendix

Appendix A: Integration method

The method described in this section is taken from Ref. [13] and applied to our specific case: the 2D Lugiato Lefever equation numerical integration. This method is pseudospectral and second-order accurate on time. In general, we can write our equation for each Fourier mode E_q as:

$$\partial_t E_q(t) = -\alpha_q E_q(t) + \Phi_q(t) \quad (\text{A.1})$$

where, for the LLE, $\alpha_q = 1 + i\theta + iq^2$ and $\Phi_q(t)$ is the amplitude of the nonlinear term in this equation. The amplitudes $\Phi_q(t)$ are computed by performing the inverse Fourier transform of $E_q(E(\vec{x}, t))$, then calculating the nonlinear term in real space and taking the direct Fourier transform of this term.

Equation (A.1) is integrated numerically in time by using a "two-step" method. For convenience in the notation, the time step at each iteration is $2\delta t$.

We start by treating exactly the linear terms by using the formal solution:

$$E_q(t) = e^{-\alpha_q t} \left(E_q(t_0) e^{\alpha_q t_0} + \int_{t_0}^t \Phi_q(s) e^{\alpha_q s} ds \right). \quad (\text{A.2})$$

Taking $t_0 = t - \delta t$ and $t = t + \delta t$ we find the following relationship:

$$\frac{E_q(t + \delta t)}{e^{-\alpha_q \delta t}} - \frac{E_q(t - \delta t)}{e^{\alpha_q \delta t}} = e^{-\alpha_q t} \int_{t - \delta t}^{t + \delta t} \Phi_q(s) e^{\alpha_q s} ds. \quad (\text{A.3})$$

If we now take the Taylor expansion of $\Phi_q(s)$ around $s = t$ for small δt , we obtain:

$$e^{-\alpha_q t} \int_{t - \delta t}^{t + \delta t} \Phi_q(s) e^{\alpha_q s} ds \approx \Phi_q(t) \frac{e^{\alpha_q \delta t} - e^{-\alpha_q \delta t}}{\alpha_q} + O(\delta t^3) \quad (\text{A.4})$$

Substituting the result of Eq. (A.4) in Eq. (A.3) we get:

$$E_q(n + 1) = e^{-2\alpha_q \delta t} E_q(n - 1) + \frac{1 - e^{-2\alpha_q \delta t}}{\alpha_q} \Phi_q(n) + O(\delta t^3) \quad (\text{A.5})$$

where $f(n) = f(t = n\delta t)$. This expression (A.5) is the so-called slaved leapfrog [14].

To use this scheme, we need the values of the field at the first two time steps. Nevertheless, following similar steps to the ones before, one can obtain an auxiliary expression:

$$E_q(n) = e^{-\alpha_q \delta t} E_q(n-1) + \frac{1 - e^{-\alpha_q \delta t}}{\alpha_q} \Phi_q(n-1) + O(\delta t^2) \quad (\text{A.6})$$

The numerical method we use provides the time evolution of the field from an initial condition by using both Eq. (A.5) and (A.6). The order is the following:

- (i) $\Phi_q(n-1)$ is calculated from $E_q(n-1)$ at real space
- (ii) We use Eq. (A.6) to obtain an approximation of $E_q(n)$.
- (iii) The nonlinear term is recalculated from this $E_q(n)$ at real space
- (iv) The field $E_q(n+1)$ is calculated from Eq. (A.5) by using $E_q(n-1)$ and $\Phi_q(n)$.

Therefore, at each iteration we get $E_q(n+1)$ from $E_q(n-1)$ and the time step is $2\delta t$. The total error is of order $O(\delta t^3)$ despite Eq. (A.6) is of order $O(\delta t^2)$. This integration method has been tested also in Ref. [13].

As our system size involves using matrix of 2048 X 2048, in order to compute (twice for each time step) the direct and inverse Fourier transform, we need an efficient code or subroutine. For our calculations, we used the Math Kernel Library from Intel (FFT DFTI), which has proven to have good precision in less time than others common libraries.

Appendix B: Linear stability analysis of stationary periodic pattern

In this appendix we describe the procedure we have used in chapter 2 to perform the linear stability analysis of the stationary periodic patterns result from a partial differential equation. This method follows the one described at [9]. As our case is a single two dimensional complex partial differential equation, we describe the method for this case.

We consider partial differential equation in a general form

$$\partial_t E(\vec{x}, t) = W(\nabla^{(2n)}, E(\vec{x}, t)) \quad (\text{B.1})$$

where $E(\vec{x}, t)$ is a two dimensional $\vec{x} = (x, y)$ complex field, $\nabla^{(2n)}$ (with n a natural number) is a two dimensional Laplacian and W is the homogeneous nonlinear operator that describes the different contributions in our equation. We consider $E_h(\vec{x})$ a spatially periodic solution that fulfills $W(\nabla^{(2n)}, E_h(\vec{x})) = 0$.

Linearizing Eq. (B.1) around the stationary solution $E_h(\vec{x})$ we obtain the equation for the fluctuations $\delta E(\vec{x}, t) = E(\vec{x}, t) - E_h(\vec{x})$:

$$\partial_t \delta E(\vec{x}, t) = \alpha(\nabla^{(2n)}, E_h(\vec{x})) \delta E + \beta(\nabla^{(2n)}, E_h(\vec{x})) \delta E^* \quad (\text{B.2})$$

where $\alpha = \delta_E[W]|_{E_h}$ and $\beta = \delta_{E^*}[W]|_{E_h}$ are the functional derivatives of W with respect to E and E^* , respectively, evaluated at E_h . These α and β depend nonlinearly on $E_h(\vec{x})$ and $\nabla^{(2n)} E_h(\vec{x})$ but do not depend on δE . For the Lugiato-Lefever equation discussed in chapter 2 we find, from Eq. 2.8, that:

$$\alpha = -(1 + i\theta) + i\nabla^2 + 2i|E_h(\vec{x})|^2 \quad \beta = iE_h^2 \quad (\text{B.3})$$

If we consider δE and δE^* independent variables, from Eq. (B.2) we obtain:

$$\partial_t \delta \vec{E} = L(E_h) \delta \vec{E} \quad \text{with} \quad \delta \vec{E} = (\delta E, \delta E^*) \quad (\text{B.4})$$

where

$$L(E_h) = \begin{pmatrix} \alpha & \beta \\ \beta^* & \alpha^* \end{pmatrix} = \begin{pmatrix} -(1 + i\theta) + i\nabla^2 + 2i|E_h(\vec{x})|^2 & iE_h^2 \\ -iE_h^{*2} & -(1 - i\theta) - i\nabla^2 - 2i|E_h(\vec{x})|^2 \end{pmatrix}. \quad (\text{B.5})$$

From Eq. (B.4), the eigenvalue problem to solve is:

$$L(E_h) \vec{\phi} = \lambda \vec{\phi} \quad (\text{B.6})$$

where λ are the eigenvalues that determine E_h stability and $\vec{\phi}$ is the eigenvector associated to the eigenvalue λ . If any eigenvalue is positive, the pattern will be unstable.

Moreover, the eigenvector associated to the positive eigenvalue indicates the spatial profile of the growing perturbation. As the coefficients of L are periodic, we can use the Bloch's theorem to find its eigenvectors and eigenvalues. Therefore, the eigenvectors $\vec{\phi}$ have the form of a plane wave times a function with the same periodicity than the pattern E_h :

$$\vec{\psi}(\vec{x}, \vec{q}) = \begin{pmatrix} e^{i\vec{q}\vec{x}} A(\vec{x}, \vec{q}) \\ e^{-i\vec{q}\vec{x}} A^*(\vec{x}, -\vec{q}) \end{pmatrix} \quad \text{where} \quad A(\vec{x} + \vec{R}, \vec{q}) = A(\vec{x}, \vec{q}) \quad (\text{B.7})$$

being \vec{R} any vector of the lattice defined by the pattern.

From the general expression of the stationary hexagonal pattern, Eq. 2.7, we write an expression for $A(\vec{x}, \vec{q})$:

$$A(\vec{x}, \vec{q}) = \sum_{m=0}^{N-1} \delta a_m(\vec{q}) e^{i\vec{k}_m^0 \vec{x}} \quad (\text{B.8})$$

where \vec{k}_m^0 are the wavevectors of the pattern. \vec{k}_0^0 is the homogeneous mode and the other $n = 1, N - 1$ are the six fundamental wavevectors and their harmonics. $\delta a_m(\vec{q})$ are the complex amplitudes that give rise to the perturbation. Using this last expression in equation (B.6) we have two general equations

$$\begin{aligned} & \alpha (\nabla^{2n}, E_h(\vec{x})) \sum_{m=0}^{N-1} \delta a_m(\vec{q}) e^{i(\vec{k}_m^0 + \vec{q})\vec{x}} \\ & + \beta (\nabla^{2n}, E_h(\vec{x})) \sum_{m=0}^{N-1} \delta a_m^*(-\vec{q}) e^{-i(\vec{k}_m^0 + \vec{q})\vec{x}} = \lambda \sum_{m=0}^{N-1} \delta a_m(\vec{q}) e^{i(\vec{k}_m^0 + \vec{q})\vec{x}} \end{aligned} \quad (\text{B.9})$$

$$\begin{aligned} & \beta^* (\nabla^{2n}, E_h(\vec{x})) \sum_{m=0}^{N-1} \delta a_m(\vec{q}) e^{i(\vec{k}_m^0 + \vec{q})\vec{x}} \\ & + \alpha^* (\nabla^{2n}, E_h(\vec{x})) \sum_{m=0}^{N-1} \delta a_m^*(-\vec{q}) e^{-i(\vec{k}_m^0 + \vec{q})\vec{x}} = \lambda \sum_{m=0}^{N-1} \delta a_m^*(-\vec{q}) e^{-i(\vec{k}_m^0 + \vec{q})\vec{x}} \end{aligned} \quad (\text{B.10})$$

For our system, one obtains:

$$\begin{aligned} & - \left(1 + i \left(\theta + \left| \vec{k}_m^0 + \vec{q} \right|^2 \right) \right) \sum_{m=0}^{N-1} \delta a_m(\vec{q}) e^{i(\vec{k}_m^0 + \vec{q})\vec{x}} \\ & + i2 \sum_{l=0}^{N-1} \sum_{m=0}^{N-1} \sum_{n=0}^{N-1} a_l a_m^* \delta a_n(\vec{q}) e^{i(\vec{k}_l^0 - \vec{k}_m^0 + \vec{k}_n^0 + c\vec{q})\vec{x}} \\ & + i \sum_{l=0}^{N-1} \sum_{m=0}^{N-1} \sum_{n=0}^{N-1} a_l a_m \delta a_n^*(-\vec{q}) e^{i(\vec{k}_l^0 + \vec{k}_m^0 - \vec{k}_n^0 - \vec{q})\vec{x}} \\ & = \lambda \sum_{m=0}^{N-1} \delta a_m(\vec{q}) e^{i(\vec{k}_m^0 + \vec{q})\vec{x}} \end{aligned} \quad (\text{B.11})$$

$$\begin{aligned}
& i \sum_{l=0}^{N-1} \sum_{m=0}^{N-1} \sum_{n=0}^{N-1} a_l^* a_m^* \delta a_n(\vec{q}) e^{-i(\vec{k}_l^0 + \vec{k}_m^0 - \vec{k}_n^0 - \vec{q})\vec{x}} \\
& - \left(1 - i \left(\theta + \left| \vec{k}_m^0 + \vec{q} \right|^2 \right) \right) \sum_{m=0}^{N-1} \delta a_m^*(-\vec{q}) e^{-i(\vec{k}_m^0 + \vec{q})\vec{x}} \\
& - i 2 \sum_{l=0}^{N-1} \sum_{m=0}^{N-1} \sum_{n=0}^{N-1} a_l^* a_m \delta a_n^*(-\vec{q}) e^{-i(\vec{k}_l^0 - \vec{k}_m^0 + \vec{k}_n^0 + \vec{q})\vec{x}} \\
& = \lambda \sum_{m=0}^{N-1} \delta a_m^*(-\vec{q}) e^{-i(\vec{k}_m^0 + \vec{q})\vec{x}}
\end{aligned} \tag{B.12}$$

That are the equations to solve to obtain the eigenvalues. We can see it more clear if we group terms with the same exponential:

$$\begin{aligned}
& \left[-(1 + i\theta) - i \left| \vec{k}_n^0 \pm \vec{q} \right|^2 \delta a_n(\vec{q}) + i 2 \left[\sum_{l=0}^{N-1} \sum_{m=0}^{N-1} a_l a_m^* \delta a_{n-l+m}(\vec{q}) \right] \right. \\
& \left. + i \left[\sum_{l=0}^{N-1} \sum_{m=0}^{N-1} a_l a_m \delta a_{-n+l+m}^*(-\vec{q}) \right] \right] = \lambda \delta a_n(\vec{q}, t)
\end{aligned} \tag{B.13}$$

$$\begin{aligned}
& \left[-(1 - i\theta) + i \left| \vec{k}_n^0 \pm \vec{q} \right|^2 \delta a_n^*(-\vec{q}) - i 2 \left[\sum_{l=0}^{N-1} \sum_{m=0}^{N-1} a_l a_m^* \delta a_{n-l+m}^*(-\vec{q}) \right] \right. \\
& \left. - i \left[\sum_{l=0}^{N-1} \sum_{m=0}^{N-1} a_l a_m \delta a_{-n+l+m}(\vec{q}) \right] \right] = \lambda \delta a_n^*(-\vec{q}, t)
\end{aligned} \tag{B.14}$$

where $\delta a_{n-l+m}(\pm\vec{q}) = \delta a_j(\pm\vec{q})$ with $\vec{k}_j^0 = \vec{k}_n^0 - \vec{k}_l^0 + \vec{k}_m^0$. If we write the $\delta a_n(\pm\vec{q})$ as a vector ($\vec{\Sigma}_n(\vec{q}) \equiv (\delta a_0(\vec{q}), \dots, \delta a_{N-1}(\vec{q}), \delta a_0^*(-\vec{q}), \dots, \delta a_{N-1}^*(-\vec{q}))^T$), we can use both expressions above to reduce this to an eigenvalue problem for each value of \vec{q} :

$$M(a_m, \vec{q}) \vec{\Sigma}(\vec{q}, t) = \lambda(\vec{q}) \vec{\Sigma}(\vec{q}) \tag{B.15}$$

Thus, the stability of our stationary periodic pattern $E_h(\vec{x})$ reduce to finding the $2N$ eigenvalues $\lambda_n(\vec{q})$ of the matrix $M(a_m, \vec{q})$ for each value of \vec{q} . This eigenvalues determine the stability of the pattern against perturbations containing any set of wavevectors $\vec{k}_m^0 \pm \vec{q}$.

Note that, as we have seen, Bloch theorem tells us that perturbations can be written as superposition of Bloch waves (B.7), and that each Bloch wave with different \vec{q} is independent, except with \vec{q} and $-\vec{q}$ due to a coupling between δE and E^* .

Furthermore, we can use the *reduced zone scheme* from solid state physics to say that any perturbation with a vector \vec{q}' outside the first Brillouin zone is equivalent to another with a vector $\vec{q} = \vec{q}' + \vec{k}_m^0$ inside. Therefore, to know the stability of the solution against any possible perturbation, we just need to analyse the first Brillouin zone. In addition, as \vec{q} and $-\vec{q}$ are simultaneously contained in $\vec{\Sigma}(\vec{q})$, only one half of the first Brillouin zone must

be explored. In fact, due to the hexagonal symmetry of the pattern, only a 1/6 of the first Brillouin zone must be explored (see this symmetry in Fig. 2.7).

Note that, following this method, the computational cost is directly related with N (the number of modes included in the analysis). Therefore, with this approach the matrices to diagonalize are much smaller size than comparing with a method using the real space directly. Furthermore, as \vec{q} is a free variable in this analysis, all perturbations are possible no matter how small $|\vec{q}|$ is, without any increase of the computational cost.

Regarding to the measure of the error, we can use as an indicator the amplitude of the last harmonics in the truncation when considering the general form of the hexagonal pattern (2.7) and the perturbation (B.8). For our case we used $N = 295$ modes, where the last harmonics have an amplitude of order 10^{-6} . In order to check if our results for the method were correct, we compared them with previous studies that use this analysis to compute the profile of the Goldstone mode [15].

Bibliography

- [1] Cross, M. C. and Hohenberg, P. C. *Reviews of modern physics*, 65 (3), 851. (1993)
- [2] Labeyrie, Guillaume, et al. *Nature Photonics* 8.4 (2014): 321-325.
- [3] Verkerk, P. et al. *Europhys. Lett.* 26, 171–176 (1994).
- [4] Inouye, S. et al. *Science* 285, 571–574 (1999).
- [5] Bonifacio, R. DeSalvo, L. *Nucl. Instrum. Methods Phys. Res. Sect. A* 341, 360–362 (1994).
- [6] Tesio E., Robb G. R. M., Oppo G.-L., Gomes P. M., Ackemann T., Labeyrie G., Kaiser R. and Firth W. J. *Phil. Trans. R. Soc. A*.37220140002 (2014)
- [7] Kuramoto, Yoshiki. H. Araki (ed.). *Lecture Notes in Physics, International Symposium on Mathematical Problems in Theoretical Physics*. 39. Springer-Verlag, New York. p. 420. (1975)
- [8] F.T. Arecchi, S. Boccaletti and P.L. Ramazza, *Phys. Rep.* 318, 1-83 (1999).
- [9] Gomila, Damià. "Dynamics of spatial structures in nonlinear optics." (2003).
- [10] L.A. Lugiato and R. Lefever, *Phys. Rev. Lett.* 58, 2209 (1987).
- [11] A.J. Scroggie, W.J. Firth, G.S. McDonald, M. Tlidi, R. Lefever and L.A. Lugiato, *Chaos, Solitons Fractals* 4, 1323 (1994).
- [12] Walgraef, Daniel. *Springer Science Business Media*, (2012).
- [13] Montagne, Raúl, et al. *Physical Review E* 56.1: 151. (1997)
- [14] U. Frisch, Z. S. She, and O. Thual, *J. Fluid Mech.* 168, 221 (1986).
- [15] Gomila, Damià and Colet, P. *Physical review. E, Statistical, nonlinear, and soft matter physics*. 66. 046223. 10.1103/PhysRevE.66.046223. (2002)